Matrix-free TriGlobal adjoint stability analysis of compressible Navier–Stokes equations

Yuya Ohmichi *, Kento Yamada

Aeronautical Technology Directorate, Japan Aerospace Exploration Agency, 7-44-1 Jindaiji-Higashi, Chofu, Tokyo 182-8522, Japan

A B S T R A C T

A numerical method for TriGlobal (i.e., fully three-dimensional) adjoint stability analysis for compressible flows was developed and is presented in this paper. The developed method solves the adjoint stability problem using a matrix-free method based on Krylov-Schur method and a time-stepping approach. Because of the low memory (RAM) requirement of the matrix-free approach, the developed method can analyze fully three-dimensional flows that are difficult to analyze with conventional matrix-based methods. To perform time-stepping on the adjoint variables, the adjoint equations, including appropriate boundary conditions for the compressible Navier–Stokes equations, were derived. The equations were discretized using a finite compact difference method, and time integration was conducted using the three-step third-order Runge–Kutta method. A flow field around a two-dimensional square cylinder and a cubic cavity flow were analyzed using the developed method, and it was confirmed that the method reproduces the dominant instabilities reported in the literature. In addition, in the square cylinder flow analysis, the receptivity and sensitivity regions of the secondary wake mode, which corresponds to far wake instability, were clarified. Finally, the TriGlobal direct and adjoint stabilities of compressible flows over a finite width cavity were analyzed for the first time, and it was proven that large-scale adjoint stability analysis can be performed with the developed method. The results also show that instability phenomena similar to those obtained with BiGlobal stability analysis appear, but sidewall effects exist.

1. Introduction

Global stability analysis is an effective approach for investigating linear instability with respect to the base state of non-linear flows [1,2]. In global stability analysis, the dynamic behavior of a small perturbation superimposed on a steady base flow is clarified by eigenvalue analysis of the linearized Navier–Stokes equations. The dynamic behavior of the small perturbation is expressed as a superposition of eigenmodes (referred to as global modes), and unstable modes can be identified from the growth rate. Furthermore, in recent years, methods for analyzing the receptivity and sensitivity of instability phenomena by calculating the global modes of the corresponding adjoint equations have been studied [3–6]. In this paper, we refer to the global modes of linearized and adjoint equations as direct and adjoint modes, respectively. By calculating the adjoint modes, it is possible to identify the regions that are highly receptive to external forces called wavemakers [4], which

---

* Corresponding author.
   E-mail address: ohmichi.yuya@jaxa.jp (Y. Ohmichi).

strongly influence the temporal dynamics (namely growth rate and frequency) of the instability. Therefore, adjoint stability analysis is considered to be effective in understanding the nature of the flow field and its application to flow control.

There are two major approaches toward global stability analysis. One is the matrix-forming approach, which explicitly assembles the Jacobian matrix of the linearized Navier–Stokes equations. With this approach, the global modes can be calculated in a relatively short computation time (CPU time) by effectively utilizing the sparsity of the Jacobian matrix. In addition, adjoint stability analysis can be performed easily with the Jacobian matrix. Therefore, most studies on the adjoint global stability analysis have been conducted using the matrix-forming approach [4–7]. However, it requires a large amount of computational memory (RAM) to assemble and invert the Jacobian required by eigenvalue problem solvers. The large memory requirement makes it difficult to perform large-scale flow analysis with three non-homogeneous spatial directions, referred to as TriGlobal stability analysis. This approach is suitable for relatively small-scale analysis with two non-homogeneous spatial directions, referred to as BiGlobal stability analysis. The other main approach is the matrix-free approach. This approach does not need to assemble the Jacobian matrix explicitly and only requires a small amount of RAM. Therefore, this approach has a great advantage of being applicable to large-scale TriGlobal stability analysis. Many studies on the direct global stability analysis have been conducted using this approach [8–14] but few studies have conducted on the adjoint global stability analysis.

Most studies on global stability analysis have investigated incompressible fluid flow, but in recent years, those on compressible fluid flow have been increasing [9–17]. In a previous study, Ohmichi and Suzuki [10] developed the TriGlobal direct stability analysis method for the compressible Navier–Stokes equations. Their method is effective for large-scale TriGlobal stability analysis because it has a matrix-free property based on the time-stepping approach [18,8] and the high-order spatial accuracy of the finite compact difference method [19]. In this paper, we propose a TriGlobal adjoint stability analysis method taking the matrix-free approach, which is an extension of that by Ohmichi and Suzuki [10].

The matrix-free approach for adjoint global stability analysis can be further classified into two approaches: discrete and continuous. The discrete approach includes the automatic differentiation (AD) and the modular approach [15], which are being studied to minimize the additional human effort required to compute the adjoint system. However, AD approach is not used for adjoint global stability analysis since the adjoint analysis code provided by the general AD softwares is not efficient enough for large-scale fluid problems and careful tuning of the code is required to obtain good computational efficiency [20]. The modular approach was recently proposed by Fosas de Pando et al. [15] and the verification of its applicability to TriGlobal analysis is desired. The continuous approach, investigated in this study, requires the cumbersome task of deriving the governing equations and boundary conditions of the adjoint system analytically. Furthermore, because this approach discretizes the linearized equation and the adjoint equation separately, it is non-trivial whether the adjoint mode corresponding to the direct mode can be obtained. Note that mathematically, the eigenvalues of direct and adjoint modes are complex conjugates of each other. Due to these problems, adjoint stability analysis based on the matrix-free continuous approach has not yet been applied to compressible fluid flows. However, once these problems are solved, it will be relatively easy to extend Ohmichi and Suzuki's method [10], which is based on the matrix-free approach and the finite compact difference method, to adjoint stability analysis.

The objective of this study was to develop and verify a TriGlobal adjoint stability analysis method based on the matrix-free continuous approach. The adjoint equations of the compressible Navier-Stokes equations and appropriate boundary conditions are derived. We demonstrate that the developed method produces accurate adjoint modes and is applicable to large-scale TriGlobal adjoint stability analysis through three analyses: of a flow around a two-dimensional square cylinder, a cubic cavity flow, and a fully three-dimensional open cavity flow.

2. Global linear stability

2.1. Direct modes

The linearized Navier–Stokes equations can be written as

$$\frac{d\boldsymbol{q}'}{dt} = \boldsymbol{J}\boldsymbol{q}', \tag{1}$$

where $\boldsymbol{q}'$ denotes the small-amplitude perturbations of the variables $\boldsymbol{q} = \begin{bmatrix} \rho & \boldsymbol{m} & p \end{bmatrix}^T$ and ρ, $\boldsymbol{m}$, and p are density, momentum vector, and pressure, respectively. The momentum vector is composed of $\boldsymbol{m} = \begin{bmatrix} m_1 & m_2 & m_3 \end{bmatrix}^T = \begin{bmatrix} \rho u & \rho v & \rho w \end{bmatrix}^T$ where u, v, and w are the velocity in x, y and z directions. The matrix $\boldsymbol{J}$ is the Jacobian operator obtained by linearizing the nonlinear Navier–Stokes equations about the baseflow $\bar{\boldsymbol{q}}$. The dimension of $\boldsymbol{J}$ is determined by the number of cells and variables and therefore becomes large. The baseflow $\bar{\boldsymbol{q}}$ is the equilibrium solution of the nonlinear Navier–Stokes equations. Assuming normal mode decomposition, the solution of Equation (1) can be written in the form

$$\boldsymbol{q}'(\boldsymbol{x}, t) = \sum_j a_j \hat{\boldsymbol{q}}_j(\boldsymbol{x}) \exp(\lambda_j t), \tag{2}$$

where

$$\lambda_j = \sigma_j + i\omega_j. \tag{3}$$

$\boldsymbol{x} = (x,\ y,\ z)$ and t are position and time, respectively, $\hat{\boldsymbol{q}}_j(\boldsymbol{x})$ describes the spatial distribution of the mode amplitude, and the real part σ_j and imaginary part ω_j of λ_j are the growth rate and angular frequency, respectively. a_j is a coefficient determined by the initial state. The eigenmode $(\hat{\boldsymbol{q}}_j,\ \lambda_j)$ can be obtained by solving the following eigenvalue problem, which is obtained by substituting Equation (2) into (1).

$$\boldsymbol{J}\hat{\boldsymbol{q}} = \lambda\hat{\boldsymbol{q}}. \tag{4}$$

We refer to the eigenmode $(\hat{\boldsymbol{q}}_j,\ \lambda_j)$ as the direct mode.

The decomposition of the solution of the perturbations (2) tells us that the behavior of the perturbations is attributed to its time evolution, spatial distribution, and initial amplitude. That is, the spatial distribution and its dynamic behavior of linear instabilities can be understood by solving (4).

2.2. Adjoint modes

We define the adjoint operator $\boldsymbol{J}^*$ associated with $\boldsymbol{J}$, which satisfies

$$\langle \boldsymbol{J}\boldsymbol{q}_1, \boldsymbol{q}_2 \rangle = \langle \boldsymbol{q}_1, \boldsymbol{J}^*\boldsymbol{q}_2 \rangle \tag{5}$$

for arbitrary vectors $\boldsymbol{q}_1$ and $\boldsymbol{q}_2$. The inner product is defined as

$$\langle \boldsymbol{q}_1, \boldsymbol{q}_2 \rangle = \int_\Omega \boldsymbol{q}_2^H \boldsymbol{q}_1 dV, \tag{6}$$

where Ω is control volume and superscript H is a conjugate transpose operator. In Section 3.3, we define the adjoint Navier–Stokes equations using the adjoint operator $\boldsymbol{J}^*$.

The adjoint Navier–Stokes equations can be written in terms of $\boldsymbol{J}^*$ as

$$\frac{d\boldsymbol{q}^*}{dt} = \boldsymbol{J}^*\boldsymbol{q}^*, \tag{7}$$

where $\boldsymbol{q}^* = \begin{bmatrix} \rho^* & \boldsymbol{m}^* & p^* \end{bmatrix}^T$ denotes the adjoint variables. In the same manner as for direct modes, the adjoint mode $(\boldsymbol{q}_j^+,\ \lambda_j^+)$ is defined as the solution of the following eigenvalue problem:

$$\boldsymbol{J}^*\boldsymbol{q}^+ = \lambda^+\boldsymbol{q}^+. \tag{8}$$

2.3. Numerical methods for eigenvalue problem

In this section, we describe the numerical methods to obtain the direct mode, which is the solution of Equation (4). The adjoint modes can be obtained by solving Equation (8) in the same manner.

Equation (4) is a large-scale eigenvalue problem which is difficult to solve because a large amount of RAM is required to construct the matrix $\boldsymbol{J}$ in the case of TriGlobal stability analysis. This difficulty can be avoided by solving the eigenvalue problem with the time-stepping approach proposed by Eriksson and Rizzi [18] and Chiba [8]. In the time-stepping approach, by combining the time evolution of linearized equations (1) and the Arnoldi method [21], it is possible to obtain global modes using less RAM without explicitly constructing $\boldsymbol{J}$. This method is briefly described below.

2.3.1. Arnoldi method

To solve the large-scale eigenvalue problem in (4), the Arnoldi method induces a Krylov subspace K_m composed of m vectors:

$$K_m = \left\{ \boldsymbol{v},\ \boldsymbol{J}\boldsymbol{v},\ \boldsymbol{J}^2\boldsymbol{v}, \cdots,\ \boldsymbol{J}^{m-1}\boldsymbol{v} \right\}, \tag{9}$$

where $\boldsymbol{v}$ is an arbitrary initial vector. Then, the matrix $\boldsymbol{J}$ is projected onto the Krylov subspace K_m, resulting in the following eigenvalue problem with the projected $\boldsymbol{J}$:

$$\boldsymbol{V}_m^T \boldsymbol{J} \boldsymbol{V}_m \boldsymbol{z} = \lambda^{(m)} \boldsymbol{z}, \tag{10}$$

where $\boldsymbol{V}_m$ is a matrix composed of the orthonormal bases of K_m. The dimension of the eigenvalue problem in (10) is m and is small enough to solve. Then, the eigenvalues and eigenvectors of $\boldsymbol{J}$ are calculated by

$$\lambda = \lambda^{(m)} \text{ and } \hat{\boldsymbol{q}} = \boldsymbol{V}_m \boldsymbol{z}. \tag{11}$$

These obtained m eigenmodes are the approximate eigenmodes of $\boldsymbol{J}$ with larger absolute eigenvalues. The approximate eigenmodes converge to the true eigenmodes of $\boldsymbol{J}$ as m increases [22]. However, it is often not possible to use a sufficiently large m because it results in an intractable RAM requirement. To avoid this difficulty, we used the Krylov–Schur method [23], a variation of the Arnoldi method. This method generates accurate global modes with small m by utilizing an effective restart strategy. For details, see Stewart [23].

2.3.2. Time-stepping approach

The Arnoldi method tends to produce eigenmodes with larger absolute eigenvalues, although we are interested in the eigenmodes with larger growth rates for the stability analysis. To obtain the eigenmodes with larger growth rate, the following eigenvalue problem is solved instead of (4):

$$\boldsymbol{P}\boldsymbol{w} = \lambda_P \boldsymbol{w}, \tag{12}$$

where

$$\boldsymbol{P} = \exp(\boldsymbol{J}\Delta t). \tag{13}$$

With this transformation, the relation of eigenmodes of $\boldsymbol{P}$ and $\boldsymbol{J}$ is

$$\lambda_P = \exp(\lambda \Delta t) \text{ and } \boldsymbol{w} = \hat{\boldsymbol{q}}. \tag{14}$$

To solve (12) with the Arnoldi method, we must calculate the matrix-vector product $\boldsymbol{P}\boldsymbol{v}$. To obtain $\boldsymbol{P}\boldsymbol{v}$, the time-stepping approach uses the fact that Equation (1) leads to

$$\boldsymbol{v}(\Delta t) = \boldsymbol{P}\boldsymbol{v}(0). \tag{15}$$

That is, the matrix-vector product $\boldsymbol{P}\boldsymbol{v}$ can be obtained via the time integration of (1) from time $t = 0$ to $t = \Delta t$ with an initial state $\boldsymbol{v}(0) = \boldsymbol{v}$, and the matrix $\boldsymbol{J}$ need not be explicitly constructed (i.e., matrix-free). The eigenvalue problem for adjoint analysis of (8) can be solved in the same way.

2.3.3. Convergence criterion

As a convergence criterion of the obtained eigenmodes, the following formula can be used.

$$||\boldsymbol{P}\boldsymbol{w} - \lambda_P \boldsymbol{w}|| < |\lambda_P| \cdot \delta_{\text{tol}}, \tag{16}$$

where $|| \cdot ||$ is Euclidean norm. In this paper, we set δ_{tol} to 10^{-6}. A detailed explanation of the evaluation for Equation (16) can be found in Lehoucq et al. [24].

3. Governing equations

3.1. Nonlinear Navier–Stokes equations

The nonlinear compressible Navier–Stokes equations are written as

$$\frac{\partial \rho}{\partial t} = -\nabla \cdot \boldsymbol{m}, \tag{17}$$

$$\frac{\partial \boldsymbol{m}}{\partial t} = -\nabla \cdot (\boldsymbol{m} \otimes \boldsymbol{u}) - \nabla p + \nabla \cdot \boldsymbol{\tau}, \tag{18}$$

$$\frac{\partial p}{\partial t} = -\nabla \cdot (p\boldsymbol{u}) - (\gamma - 1)(p\nabla \cdot \boldsymbol{u} - \nabla \cdot \boldsymbol{Q} - \text{tr}(\boldsymbol{\tau}(\nabla \otimes \boldsymbol{u}))), \tag{19}$$

where γ is the specific heat ratio which is set to 1.4 in this paper, ∇ is a spatial differential operator, $\cdot$ is a dot product operator, $\otimes$ is a direct product operator, and tr( ) is a trace operator. Viscous stress tensor $\boldsymbol{\tau}$ and a heat flux $\boldsymbol{Q}$ are written as

$$\boldsymbol{\tau} = \frac{\mu}{Re}(\nabla \otimes \boldsymbol{u} + (\nabla \otimes \boldsymbol{u})^T - \frac{2}{3}\nabla \cdot \boldsymbol{u}), \tag{20}$$

$$\boldsymbol{Q} = \frac{\mu}{(\gamma - 1)Ma^2 RePr}\nabla T, \tag{21}$$

where Ma, Re and Pr are the Mach number, Reynolds number, and Prandtl number, respectively. Viscous coefficient μ obeys Sutherland's equation written as

$$\mu = C_1 \frac{T^{\frac{3}{2}}}{T + C_2}, \tag{22}$$

where $C_1 = 1.458 \times 10^{-6}$ and $C_2 = 110.4$. The temperature T can be calculated by

$$T = \gamma Ma^2 \frac{p}{\rho}. \tag{23}$$

3.2. Linearized Navier–Stokes equations

Taking Fréchet derivatives of Eqs. (17)–(19), linearized Navier–Stokes equations are derived as

$$\frac{\partial \rho'}{\partial t} = -\nabla \cdot \boldsymbol{m}', \tag{24}$$

$$\frac{\partial \boldsymbol{m}'}{\partial t} = -\nabla \cdot (\boldsymbol{m}' \otimes \bar{\boldsymbol{u}} + \bar{\boldsymbol{m}} \otimes \boldsymbol{u}')$$
$$-\nabla p' + \nabla \cdot \boldsymbol{\tau}', \tag{25}$$

$$\frac{\partial p'}{\partial t} = -\nabla \cdot (p' \bar{\boldsymbol{u}} + \bar{p} \boldsymbol{u}')$$
$$-(\gamma - 1)(p' \nabla \cdot \boldsymbol{u} + \bar{p} \nabla \cdot \boldsymbol{u}' - \nabla \cdot \boldsymbol{Q}' - \text{tr}(\boldsymbol{\tau}'(\nabla \otimes \bar{\boldsymbol{u}}) + \boldsymbol{\tau}(\nabla \otimes \boldsymbol{u}'))), \tag{26}$$

where ρ', $\boldsymbol{m}'$, p', and $\boldsymbol{u}'$ are the perturbations of the density, momentum vector, pressure, and velocity vector, respectively, and $\bar{\rho}$, $\bar{\boldsymbol{m}}$, $\bar{p}$, and $\bar{\boldsymbol{u}}$ are those of the baseflow. The perturbations of viscous stress tensor $\boldsymbol{\tau}'$ and heat flux $\boldsymbol{Q}'$ are written as

$$\boldsymbol{\tau}' = \frac{\bar{\mu}}{Re}(\nabla \otimes \boldsymbol{u}' + (\nabla \otimes \boldsymbol{u}')^T - \frac{2}{3}\nabla \cdot \boldsymbol{u}')$$
$$+\frac{\mu'}{Re}(\nabla \otimes \bar{\boldsymbol{u}} + (\nabla \otimes \bar{\boldsymbol{u}})^T - \frac{2}{3}\nabla \cdot \bar{\boldsymbol{u}}), \tag{27}$$

$$\boldsymbol{Q}' = \frac{1}{(\gamma - 1)Ma^2 Re Pr}(\bar{\mu}\nabla T' + \mu'\nabla \bar{T}), \tag{28}$$

where T', and $\bar{T}$ are the perturbation and baseflow variables of temperature, respectively. Furthermore, viscous coefficient μ' is written as

$$\mu' = \frac{d\mu}{dT}T'$$
$$= C_1 \frac{\bar{T}^{\frac{1}{2}}}{\bar{T} + C_2}\left(\frac{3}{2} - \frac{1}{\bar{T} + C_2}\right)T'. \tag{29}$$

$\boldsymbol{u}'$ and T' are calculated as

$$\boldsymbol{u}' = \frac{\boldsymbol{m}'}{\bar{\rho}} - \frac{\bar{\boldsymbol{m}}}{\bar{\rho}^2}\rho', \tag{30}$$

$$T' = \gamma Ma^2 \left(\frac{p'}{\bar{\rho}} - \frac{\bar{p}}{\bar{\rho}^2}\rho'\right). \tag{31}$$

3.3. Adjoint Navier–Stokes equations

To specifically obtain adjoint Navier–Stokes equations, we can derive them using integration by parts according to the definition of the inner product (6). Integrating (5) by parts, we obtain

$$\int_{\Omega} \boldsymbol{q}_2^H (\boldsymbol{J} \boldsymbol{q}_1)dV = \int_{\Omega} (\boldsymbol{J}^* \boldsymbol{q}_2)^H \boldsymbol{q}_1 dV + b. \tag{32}$$

The second term of the right hand side, b, is called the boundary term. According to the definition of the adjoint operator, $b = 0$ when $\boldsymbol{J}$ is continuous and linear. Then, we must set the boundary conditions of the adjoint system so that the boundary term is zero with the boundary condition of the direct system.

Adjoint Navier–Stokes equations are derived in the form of solving for time in the forward direction as

$$\frac{\partial \rho^*}{\partial t} = -\frac{\gamma \bar{p}}{\bar{\rho}}\bar{\boldsymbol{u}} \cdot \nabla p^* - (\gamma - 1)\frac{p^*}{\bar{\rho}}\bar{\boldsymbol{u}} \cdot \nabla \bar{p} - \bar{\boldsymbol{u}} \cdot (\bar{\boldsymbol{u}} \cdot \nabla)\boldsymbol{m}^*$$
$$-\frac{\bar{\boldsymbol{u}}}{\bar{\rho}} \cdot (\nabla \cdot \sigma^*) - \frac{\bar{p}}{\bar{\rho}}(s_{visc}^* + s_{heat}^*), \tag{33}$$

$$\frac{\partial \boldsymbol{m}^*}{\partial t} = \bar{\boldsymbol{u}} \cdot (\boldsymbol{\nabla} \otimes \boldsymbol{m}^* + (\boldsymbol{\nabla} \otimes \boldsymbol{m}^*)^T) + \boldsymbol{\nabla} \rho^* + \gamma \frac{\bar{p}}{\bar{\rho}} \boldsymbol{\nabla} p^*$$

$$+ (\gamma - 1) \frac{\rho^*}{\bar{\rho}} \boldsymbol{\nabla} \bar{p} + \frac{1}{\bar{\rho}} \boldsymbol{\nabla} \cdot \sigma^*, \tag{34}$$

$$\frac{\partial p^*}{\partial t} = \boldsymbol{\nabla} \cdot \boldsymbol{m}^* + \bar{\boldsymbol{u}} \cdot \boldsymbol{\nabla} p^*$$

$$- (\gamma - 1)(\boldsymbol{\nabla} \cdot \bar{\boldsymbol{u}}) p^* + s_{visc}^* + s_{heat}^*, \tag{35}$$

where ρ^*, $\boldsymbol{m}^*$, and p^* are adjoint density, momentum vector, and pressure, respectively. σ^*, $\boldsymbol{\tau}^*$, s_{visc}^*, and s_{heat}^* are terms from the viscous stress and heat conduction. They are written as

$$\sigma^* = \boldsymbol{\tau}^* - 2(\gamma - 1)\bar{\boldsymbol{\tau}} p^*, \tag{36}$$

$$\boldsymbol{\tau}^* = \frac{\bar{\mu}}{Re} \left(\boldsymbol{\nabla} \otimes \boldsymbol{m}^* + (\boldsymbol{\nabla} \otimes \boldsymbol{m}^*)^T - \frac{2}{3} \boldsymbol{\nabla} \cdot \boldsymbol{m}^* \right), \tag{37}$$

$$s_{visc}^* = -\frac{\bar{T}}{\bar{p}} \frac{d\mu}{dT} \operatorname{tr} \left((\boldsymbol{\nabla} \otimes \boldsymbol{m}^* - (\gamma - 1)(\boldsymbol{\nabla} \otimes \bar{\boldsymbol{u}}) p^*) \cdot \frac{\bar{\boldsymbol{\tau}}}{\bar{\mu}} \right), \tag{38}$$

$$s_{heat}^* = \frac{\gamma}{\bar{\rho} Pr Re} \left(\boldsymbol{\nabla} \cdot (\bar{\mu} \boldsymbol{\nabla} p^*) - \frac{d\mu}{dT} \boldsymbol{\nabla} \bar{T} \cdot \boldsymbol{\nabla} p^* \right). \tag{39}$$

We found that the derived equations consistent with the equations for optimal flow control simulations obtained by Otero et al. [25].

Furthermore, the boundary term is derived as

$$b = b_{Euler} + b_{visc} + b_{heat}, \tag{40}$$

where,

$$b_{Euler} = \int_{\partial \Omega} (\rho^* \boldsymbol{m}' + \boldsymbol{m}^* p' + \boldsymbol{m}^* \cdot (\boldsymbol{m}' \otimes \bar{\boldsymbol{u}} + \bar{\boldsymbol{m}} \otimes \boldsymbol{u}') + p^* (p' \bar{\boldsymbol{u}} + \gamma \bar{p} \boldsymbol{u}')) \cdot d\boldsymbol{A}, \tag{41}$$

$$b_{visc} = \int_{\partial \Omega} (\boldsymbol{\tau}' \boldsymbol{m}^* - \boldsymbol{\tau}^* \boldsymbol{u}' + 2(\gamma - 1) p^* \bar{\boldsymbol{\tau}} \boldsymbol{u}') \cdot d\boldsymbol{A}, \tag{42}$$

$$b_{heat} = \int_{\partial \Omega} \left((\gamma - 1) p^* \boldsymbol{Q}' - \boldsymbol{\nabla} p^* \frac{\bar{\mu}}{Ma^2 Re Pr} T' \right) \cdot d\boldsymbol{A}. \tag{43}$$

$\partial \Omega$ is the boundary of Ω. Substituting the direct boundary conditions into the boundary term, we can appropriately derive the adjoint boundary conditions. In Section 4.2, we actually derive some examples of them.

4. Fluid simulation

4.1. Spatial and temporal discretizations

In this analysis, it is necessary to implement the spatial and temporal discretizations of three sets of equations: nonlinear, linearized, and adjoint Navier–Stokes equations. The baseflow is obtained as a steady solution of the nonlinear equations, and for eigensystem analysis with the time-stepping approach described in Section 2.3.2, the time evolution calculations of linearized and adjoint equations are also required. To handle the discretization of these three sets of equations in a unified manner and to facilitate coding, we used the sixth-order compact difference method [19,26] and the eighth-order implicit filter [27] to discretize the spatial derivatives. The three-step third-order total variation diminishing Runge–Kutta scheme [28] was used for the time discretization.

4.2. Boundary treatment

4.2.1. Isothermal no-slip wall boundary

The boundary conditions of an isothermal no-slip wall for nonlinear and linearized Navier–Stokes equations (17)–(19) and (24)–(26) are given as

$$\boldsymbol{u} = \boldsymbol{0}, \ T = T_w, \tag{44}$$

and

$$\boldsymbol{u}' = \boldsymbol{0}, \ T' = 0, \tag{45}$$

where T_w is constant temperature at the wall. Substituting (44) and (45) into (40), the boundary term is written as

$$b = \int_{\partial\Omega} \left(\boldsymbol{m}^* p' + \boldsymbol{\tau}' \boldsymbol{m}^* + (\gamma - 1) p^* \boldsymbol{Q}' \right) \cdot d\boldsymbol{A}. \tag{46}$$

The adjoint boundary conditions of the isothermal no-slip wall such that (46) becomes zero are

$$\boldsymbol{m}^* = \boldsymbol{0}, \ p^* = 0. \tag{47}$$

In practical simulations, following Neumann boundary conditions for the pressure are often imposed,

$$\frac{\partial p}{\partial x_n} = 0, \ \frac{\partial p'}{\partial x_n} = 0, \tag{48}$$

where $\partial/\partial x_n$ is a partial derivative operator normal to the wall and hereinafter the subscript n indicates the component normal to a boundary. These conditions are obtained from the wall-normal momentum equations (18) and (25) respectively by assuming the viscous effect is negligible at the wall. By making the same assumption in (34) and substituting (48) to (34), only the second and third terms on the right-hand side of (34) remain and a practical boundary condition for the adjoint density corresponding to the Neumann boundary condition for the direct pressure can be obtained as

$$\frac{\partial \rho^*}{\partial x_n} = -\gamma \frac{\bar{p}}{\bar{\rho}} \frac{\partial p^*}{\partial x_n}. \tag{49}$$

4.2.2. Adiabatic no-slip wall boundary

The boundary conditions of an adiabatic no-slip wall for nonlinear and linearized Navier–Stokes equations (17)–(19) and (24)–(26) are given as

$$\boldsymbol{u} = \boldsymbol{0}, \ \frac{\partial T}{\partial x_n} = 0, \tag{50}$$

and

$$\boldsymbol{u}' = \boldsymbol{0}, \frac{\partial T'}{\partial x_n} = 0. \tag{51}$$

Substituting (50) and (51) into (40), the boundary term is written as

$$b = \int_{\partial\Omega} \left(\boldsymbol{m}^* p' + \boldsymbol{\tau}' \boldsymbol{m}^* - \nabla p^* \frac{\bar{\mu}}{Ma^2 RePr} T' \right) \cdot d\boldsymbol{A}. \tag{52}$$

The adjoint boundary conditions of the adiabatic no-slip wall such that (52) becomes zero are

$$\boldsymbol{m}^* = \boldsymbol{0}, \ \frac{\partial p^*}{\partial x_n} = 0. \tag{53}$$

For this case, substituting (48) and (53) to (34) and assuming the viscous effect is negligible on the boundary, only the second term on the right-hand side of (34) remains and the practical boundary condition for the adjoint density becomes Neumann-type:

$$\frac{\partial \rho^*}{\partial x_n} = 0. \tag{54}$$

4.2.3. Adiabatic slip wall boundary and symmetric boundary

The boundary conditions for an adiabatic slip wall for nonlinear and linearized Navier–Stokes equations (17)–(19) and (24)–(26) are given as

$$u_n = 0, \ \frac{\partial T}{\partial x_n} = 0, \ \tau_{nj} = 0 \ (j \neq n), \tag{55}$$

and

$$u'_n = 0, \ \frac{\partial T'}{\partial x_n} = 0, \ \tau'_{nj} = 0 \ (j \neq n), \tag{56}$$

where $\tau_{nj} \ (j \neq n)$ represents components of stress tensor $\boldsymbol{\tau}$ tangential to the wall. Substituting (55) and (56) into (40), the boundary term is written as

$$b = \int_{\partial \Omega} \left(m_n^* p' + \tau_{nn}' m_n^* - \tau_{nj}^* u_j' - \frac{\partial p^*}{\partial x_n} \frac{\bar{\mu}}{Ma^2 Re Pr} T' \right) dA_n. \tag{57}$$

The adjoint boundary conditions of the adiabatic slip wall such that (57) becomes zero are

$$m_n^* = \frac{\partial p^*}{\partial x_n} = \tau_{nj}^* = 0 \ (j \neq n). \tag{58}$$

For this case, substituting (48) and (58) to (34) and assuming the viscous effect is negligible on the boundary, only the second term on the right-hand side of (34) remains and the practical boundary condition for the adjoint density also becomes Neumann-type:

$$\frac{\partial \rho^*}{\partial x_n} = 0. \tag{59}$$

The above obtained boundary conditions are equivalent to the symmetric boundary conditions.

4.2.4. Inflow and outflow boundaries

At inflow and outflow boundaries, we impose a non-reflecting boundary condition based on local one-dimensional inviscid (LODI) relations [29,30].

The LODI equations for the direct and adjoint equations in the x direction of the Cartesian coordinate system are written as

$$\frac{\partial}{\partial t} \begin{pmatrix} \rho' \\ u' \\ v' \\ w' \\ p' \end{pmatrix} = - \begin{pmatrix} \frac{1}{\bar{c}^2}[L_2' + \frac{1}{2}(L_5' + L_1')] \\ \frac{1}{2\bar{\rho}\bar{c}}(L_5' - L_1') \\ L_3' \\ L_4' \\ \frac{1}{2}(L_5' + L_1') \end{pmatrix}, \tag{60}$$

$$\frac{\partial}{\partial t} \begin{pmatrix} \rho^* \\ m_1^* \\ m_2^* \\ m_3^* \\ p^* \end{pmatrix} = - \begin{pmatrix} -\bar{c}^2 L_2^* + \bar{c}\bar{u}(L_1^* - L_5^*) \\ -\bar{c}(L_1^* - L_5^*) \\ L_3^* \\ L_4^* \\ L_1^* + L_2^* + L_5^* \end{pmatrix}, \tag{61}$$

where

$$\begin{pmatrix} L_1' \\ L_2' \\ L_3' \\ L_4' \\ L_5' \end{pmatrix} = \begin{pmatrix} \Lambda_1'(\frac{\partial}{\partial x}p' - \bar{\rho}\bar{c}\frac{\partial}{\partial x}u') \\ \Lambda_2'(\bar{c}^2\frac{\partial}{\partial x}\rho' - \frac{\partial}{\partial x}p') \\ \Lambda_3'\frac{\partial}{\partial x}v' \\ \Lambda_4'\frac{\partial}{\partial x}w' \\ \Lambda_5'(\frac{\partial}{\partial x}p' + \bar{\rho}\bar{c}\frac{\partial}{\partial x}u') \end{pmatrix}, \tag{62}$$

$$\begin{pmatrix} L_1^* \\ L_2^* \\ L_3^* \\ L_4^* \\ L_5^* \end{pmatrix} = \begin{pmatrix} \frac{\Lambda_1^*}{2\bar{c}^2}\left[\frac{\partial}{\partial x}\rho^* + (\bar{u} - \bar{c})\frac{\partial}{\partial x}m_1^* + \bar{c}^2\frac{\partial}{\partial x}p^* \right] \\ -\frac{\Lambda_2^*}{\bar{c}^2}\left(\frac{\partial}{\partial x}\rho^* + \bar{u}\frac{\partial}{\partial x}m_1^* \right) \\ \Lambda_3^*\frac{\partial}{\partial x}m_2^* \\ \Lambda_4^*\frac{\partial}{\partial x}m_3^* \\ \frac{\Lambda_5^*}{2\bar{c}^2}\left[\frac{\partial}{\partial x}\rho^* + (\bar{u} + \bar{c})\frac{\partial}{\partial x}m_1^* + \bar{c}^2\frac{\partial}{\partial x}p^* \right] \end{pmatrix}, \tag{63}$$

$$\begin{pmatrix} \Lambda_1' \\ \Lambda_2' \\ \Lambda_3' \\ \Lambda_4' \\ \Lambda_5' \end{pmatrix} = \begin{pmatrix} \bar{u} - \bar{c} \\ \bar{u} \\ \bar{u} \\ \bar{u} \\ \bar{u} + \bar{c} \end{pmatrix} \quad \text{and} \quad \begin{pmatrix} \Lambda_1^* \\ \Lambda_2^* \\ \Lambda_3^* \\ \Lambda_4^* \\ \Lambda_5^* \end{pmatrix} = \begin{pmatrix} -\bar{u} + \bar{c} \\ -\bar{u} \\ -\bar{u} \\ -\bar{u} \\ -\bar{u} - \bar{c} \end{pmatrix}. \tag{64}$$

$\bar{c}$ is speed of sound, written as $\bar{c} = \sqrt{\gamma \bar{p}/\bar{\rho}}$. L_i' and L_i^* physically correspond to amplitude variations in propagating waves at Λ_i' and Λ_i^*, respectively. In this study, we applied simple non-reflecting boundary conditions based on Eqs. (60) and (61) such that incoming components (L_i' and L_i^*) from the exterior of the computational domain are set as zero and the other components are evaluated by one-sided differences. The derivation of the above LODI relations for the adjoint equations is presented in Appendix A.
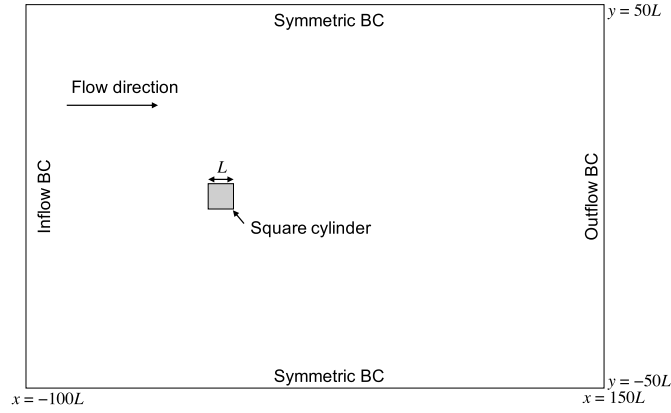
Fig. 1. Computational setup for 2D square cylinder analysis (not to scale).

Table 1
Minimum grid spacing and number of grid points of four computational grids for 2D square cylinder simulations.

Label	Δ_{min}	Number of grid points ($N_x \times N_y$)		Total number of grid points
		Whole computational domain	Square cylinder	
G1	$2.0 \times 10^{-3} L$	511×381	141×141	1.75×10^5
G2	$7.0 \times 10^{-3} L$	511×381	141×141	1.75×10^5
G3	$2.0 \times 10^{-3} L$	411×281	81×81	1.09×10^5
G4	$5.0 \times 10^{-3} L$	341×201	41×41	6.69×10^4

5. Demonstrations

5.1. 2D square cylinder flow

5.1.1. Flow conditions

First, we analyzed the low Mach number flow field around a two-dimensional square cylinder. There have been several studies on the flow around a two-dimensional cylinder using the existing technique [3–5,31]. In particular, sensitivity analysis for the unstable mode representing the Kármán vortex sheddings has been conducted, and the results have been verified experimentally [4,5]. In addition, Verma and Mittal [31] reported two instabilities, primary and secondary wake (PW and SW) instabilities, in the wake of a cylinder. In this analysis, we confirmed that the adjoint mode for the two instabilities can be obtained by the developed method.

We set the flow conditions as freestream Mach number $Ma = 0.2$ and Reynolds number based on the side length L of the square cylinder: $Re_L = 90$, 105, and 120. Fig. 1 shows the computational setup including boundary conditions. A Cartesian coordinate system was used, and the origin was placed at the center of the square cylinder. Four computational grids were used to examine the grid dependency. The details are listed in Table 1.

For the inflow boundary, the Riemann invariant boundary condition was used for the baseflow calculation, and the non-reflecting boundary condition described in Section 4.2.4 was used for the direct and adjoint stability analysis. For the outflow boundary, a constant freestream pressure was imposed, velocity and density were linearly extrapolated for the baseflow calculation, and a non-reflecting boundary condition was used for the direct and adjoint stability analysis. The symmetry boundary condition was imposed for the boundaries at $y = \pm 50L$. The adiabatic no-slip wall condition was applied to the wall of the square cylinder. For the baseflow calculation, we simulated the half domain ($y \geq 0$) with the symmetric boundary condition at $y = 0$ to obtain steady flow fields. The time step size for time integration was chosen so that Courant number, based on the minimum grid spacing and sum of the freestream speed of sound and flow velocity, is equal to 0.2. The dimension of Krylov subspace m was set to 200 and the restart strategy of Krylov-Schur method was not used in this analysis. The integration time Δt for time-stepping was set to unity. We confirmed that this condition is sufficient to obtain converged eigenmodes corresponding to PW and SW instabilities.

5.1.2. Results and discussion

Table 2 shows the grid dependency of the two least stable modes (PW and SW modes) at $Re = 120$. It can be confirmed that the eigenvalues are almost grid independent in the grids G1-G3. The changes in the growth rate and Strouhal number are $\Delta\sigma = O(10^{-4})$ and $\Delta St_L = O(10^{-4})$, respectively. The relative difference of eigenvalues in two successive grid levels is $O(10^{-3})$. Further, the direct and adjoint eigenvalues almost match. Although the eigenvalues of linearized and adjoint Navier–Stokes operators (J and J^*) are equal from a mathematical perspective, it cannot be guaranteed that those eigen-

Table 2

Eigenvalues ($\sigma \pm St_L i$) for primary and secondary wake (PW and SW) modes obtained with four different computational grids with $Re_L = 120$.

	PW mode		SW mode	
	Direct	Adjoint	Direct	Adjoint
G1	$0.1192 \pm 0.0914i$	$0.1192 \pm 0.0914i$	$0.0280 \pm 0.0978i$	$0.0280 \pm 0.0978i$
G2	$0.1193 \pm 0.0917i$	$0.1193 \pm 0.0917i$	$0.0277 \pm 0.0980i$	$0.0277 \pm 0.0980i$
G3	$0.1192 \pm 0.0915i$	$0.1192 \pm 0.0915i$	$0.0278 \pm 0.0978i$	$0.0282 \pm 0.0977i$
G4	$0.1193 \pm 0.0916i$	$0.1193 \pm 0.0916i$	$0.0275 \pm 0.0980i$	$0.0265 \pm 0.0979i$
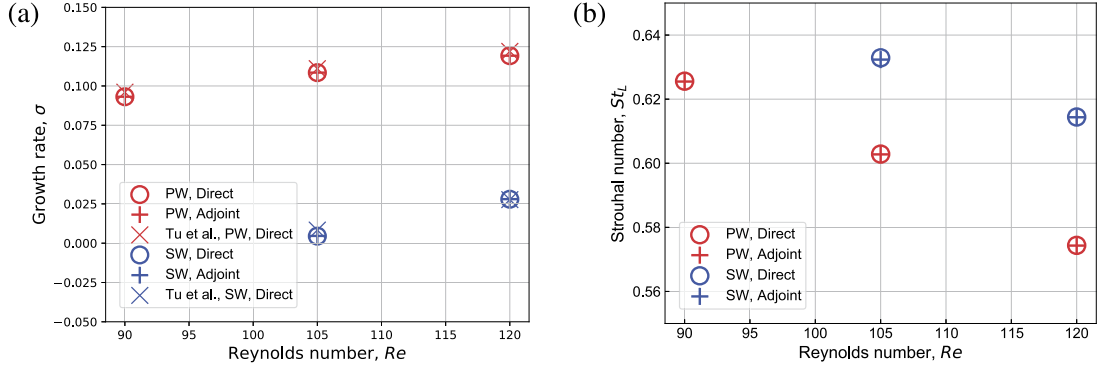
Fig. 2. Eigenvalues of primary and secondary wake modes. (a) Growth rate and (b) Strouhal number as a function of Reynolds number. The eigenvalues obtained by Tu et al. [32] are also plotted in (a).

values completely match due to the effects of discretization of the equations because $\boldsymbol{J}$ and $\boldsymbol{J}^*$ are discretized separately. Nevertheless, we can confirm from Table 2 that the direct and adjoint eigenvalues obtained with the developed method agree well when using a sufficiently fine grid. The relative difference between direct and adjoint eigenvalues is less than $O(10^{-3})$. The following results are related to the finest grid G1.

The changes of the eigenvalues of unstable modes at $Re = 90$, 105, and 120 are shown in Fig. 2. One and two unstable modes appeared at $Re = 90$ and $Re = 105$ and 120, respectively. The direct and adjoint eigenvalues of the unstable modes agree well at any Reynolds number and we confirmed that the changes of eigenvalues by Reynolds number are well captured.

Fig. 3 shows the real parts of eigenvectors for the PW and SW modes. Observing the direct eigenvector (Fig. 3a) of the PW mode, a spatial structure antisymmetric with respect to the x axis appears in the wake of the cylinder. Although not shown in the figure, the imaginary part of this eigenvector has a structure similar to that of the real part with the spatial phase shifted. This spatial pattern represents a vortex street in the wake of the cylinder. Fig. 3b shows the adjoint eigenvector of the PW mode, where the adjoint eigenvector represents the receptivity distribution. From this figure, it can be seen that the receptivity to the momentum change is large in the upper and lower surfaces of the square cylinder and the near wake region. Similar distributions have been reported in previous studies [4]. In addition, Fig. 3c shows that the SW mode corresponds to far wake instability. A similar far wake instability was previously observed in the flow past a cylinder [31] and a two-dimensional airfoil [33]. The area with large receptivity in the SW mode (Fig. 3d) is similar to that in the PW mode.

By performing the adjoint analysis, the sensitivity of the corresponding modes to local feedback of perturbation can be calculated by the following equation [4]:

$$S(x, y) = \|\hat{\boldsymbol{q}}\| \cdot \|\boldsymbol{q}^+\|, \tag{65}$$

where $\|\hat{\boldsymbol{q}}\| = \sqrt{\hat{\boldsymbol{q}}^H \hat{\boldsymbol{q}}}$ and so is $\|\boldsymbol{q}^+\|$. That is, the sensitivity takes a large value in the area where direct and adjoint modes overlap. Fig. 4a and 4b show the sensitivity distribution. Fig. 4a indicates that the PW mode is sensitive in the recirculation bubble region behind the square cylinder. The recirculation bubble is shown in Fig. 4c. Giannetti and Luchini [4] and Marquet et al. [5] conducted adjoint analysis of the incompressible flow field around a cylinder, and the results herein are consistent with their results. In addition, the present results are in good agreement with the results of a previous study in which the similar sensitivity distribution was experimentally investigated [34], which indicates that the method developed in this study correctly predicts the properties of the flow field. Interestingly, from Fig. 4b, it can be seen that the sensitivity region of the SW mode differs from the sensitivity distribution of the PW mode. That is, there are two areas of high sensitivity in the front and rear areas of the recirculation bubble, and the rear part has greater sensitivity.
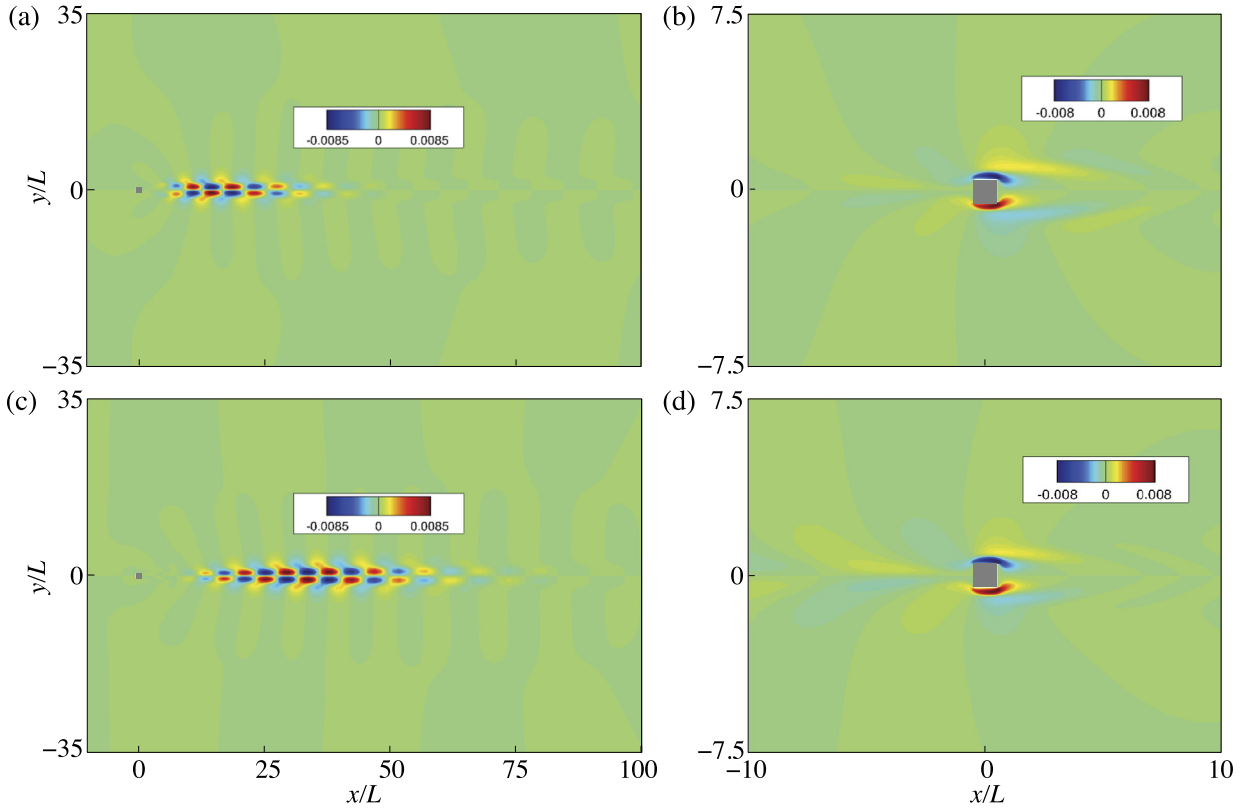
Fig. 3. Eigenvectors of (a, b) primary and (c, d) secondary wake modes. Distributions of momentum in x direction are shown. (a, c) and (b, d) show direct and adjoint modes, respectively.

5.2. 3D cubic lid-driven cavity flow

5.2.1. Flow conditions

Next, to confirm that the fully three-dimensional global mode can be analyzed by the developed method, we analyzed the cubic lid-driven cavity (LDC) flow. The cubic LDC flow is a flow in a cube consisting of one moving wall and five stationary walls, and the flow field becomes completely three-dimensional. The computational domain was set to $0 \leq x, y, z \leq 1$. The velocity distribution of the moving wall (at $y = 1$) is given by the following formula with reference to Theofilis [35]:

$$u(x, 1, z) = [1 - (2x - 1)^{16}]^2 [1 - (2z - 1)^{16}]^2. \tag{66}$$

The initial conditions for nonlinear NS simulation were set to those of a stationary fluid. The Mach number and Reynolds number based on the physical variables of the stationary fluid and velocity of the moving wall were set to $Ma = 0.2$ and $Re = 200$, respectively. Each wall condition was set to that of an isothermal no-slip wall. The computational grid was a uniform Cartesian grid with 101^3 points. The time step size for time integration was chosen so that Courant number, based on the grid spacing and sum of the acoustic speed of initial stationary fluid and maximum moving wall velocity, is equal to 0.2. The dimension of Krylov subspace m was set to 30 and the restart strategy of Krylov-Schur method was not used in this analysis. The integration time Δt for time-stepping was set to 5. We confirmed that sufficient convergence of three least stable eigenmodes is achieved with this condition.

5.2.2. Results and discussion

Theofilis [35] conducted an incompressible TriGlobal direct stability analysis of this flow field. Table 3 shows the eigenvalues of the three least stable modes obtained by the present analysis and Theofilis's analysis. The eigenvalues of the three analyses, the direct stability analysis by Theofilis and the direct and adjoint stability analyses by present methods, are in good agreement, and it can be confirmed that the relative difference is $O(10^{-3})$. Also, the relative difference between direct and adjoint eigenvalues is $O(10^{-3})$. Fig. 5 shows the direct and adjoint eigenvectors of the least stable mode (1st mode). It can be confirmed that the present method captures the fully three-dimensional spatial structure of the instability.
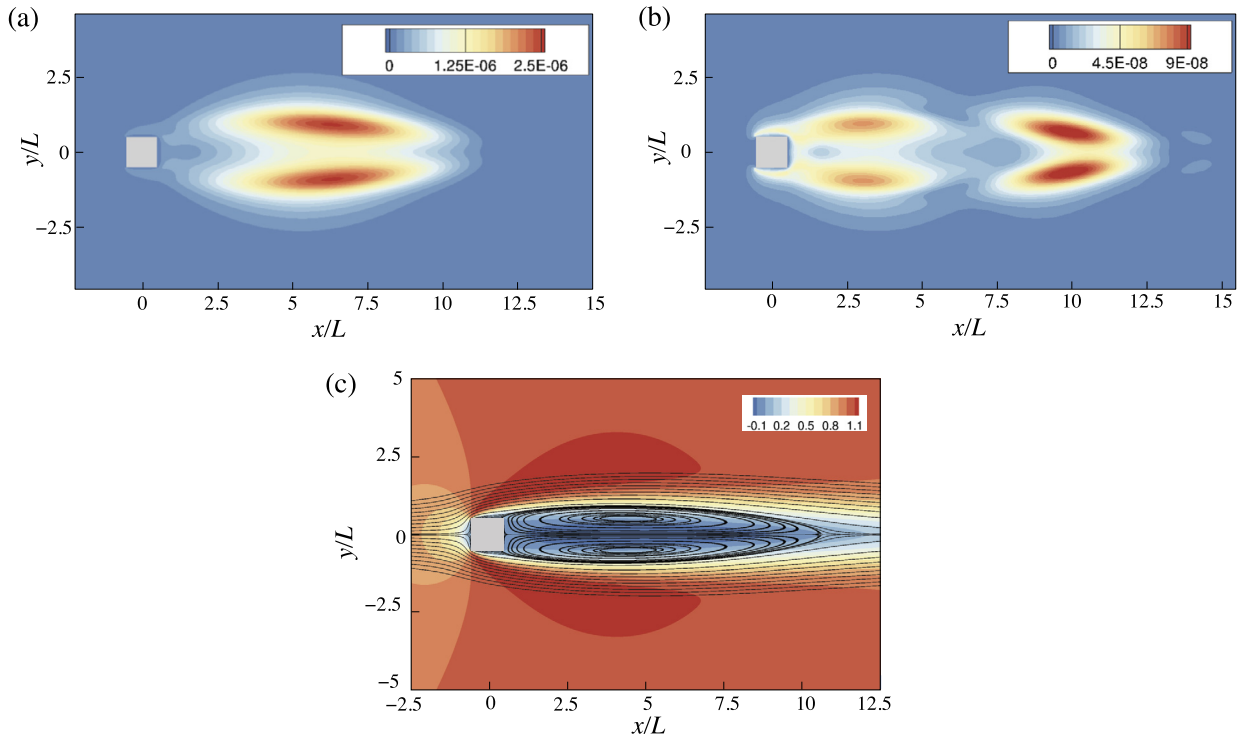
Fig. 4. Sensitivity regions of (a) primary and (b) secondary wake modes. (c) Distribution of momentum in x direction and streamlines indicating a recirculation bubble of baseflow at $Re = 120$.

Table 3
Comparison of eigenvalues ($\sigma \pm \omega i$) of cubic cavity flow analysis.

	1st mode	2nd mode	3rd mode
Theofilis [35], direct mode	$-0.4164 \pm 0.1320i$	$-0.4507 \pm 0i$	$-0.5793 \pm 0.4533i$
Present study, direct mode	$-0.4138 \pm 0.1298i$	$-0.4485 \pm 0i$	$-0.5777 \pm 0.4471i$
Present study, adjoint mode	$-0.4142 \pm 0.1297i$	$-0.4481 \pm 0i$	$-0.5766 \pm 0.4471i$

5.3. Flow over a finite-width open cavity

5.3.1. Flow conditions

In this section, we analyze a finite-width open cavity flow. There are several studies that have investigated the global stability of compressible open cavity flow [36–38]. However, they are all BiGlobal stability analyses assuming periodicity in the spanwise direction. TriGlobal stability analysis that considers the existence of sidewalls of the cavity has not been conducted due to the intractable calculation cost. Here, we demonstrate that large-scale TriGlobal direct and adjoint stability analyses can be performed using the developed method.

The computational setup is presented in Fig. 6. A Cartesian coordinate system was used, and the origin was placed at the center of the cavity leading edge. The aspect ratios of the cavity were $L/D = 2$ and $W/D = 2$, where D, L, and W are cavity depth, length, and width, respectively. The cavity was located $4D$ downstream from the leading edge of the flat-plate. The inflow boundary was placed at $10D$ upstream from the leading edge of the flat-plate. The freestream flow conditions were Mach number of $M = 0.6$ and Reynolds number based on D of $Re_D = 1500$. With these conditions, the momentum boundary layer thickness at the cavity leading edge ($x/D = 0$), obtained by the baseflow simulation, is $\theta/D = 3.2 \times 10^{-2}$. This thickness corresponds to $L/\theta = 62.5$ and $Re_\theta = 48$.

For the inflow boundary, the Riemann invariant boundary condition was used for the baseflow calculation, and non-reflecting boundary condition was used for the direct and adjoint stability analyses. For the outflow boundary, a constant freestream pressure was imposed, velocity and density were linearly extrapolated for the baseflow calculation, and a non-reflecting boundary condition was used for the direct and adjoint stability analyses. We have confirmed that by using the non-reflecting boundary condition, spurious reflections at the inflow and outflow boundaries do not appear in the eigenmodes. The flat-plate and cavity walls assumed the isothermal no-slip wall boundary condition. The wall temperature was assumed constant at the temperature of the freestream. The symmetry boundary condition was imposed for other boundaries (i.e., the sides ($y = \pm 5D$), top ($z = 10D$) and bottom ($x < -4D$ and $z = 0$) boundaries). The time step size
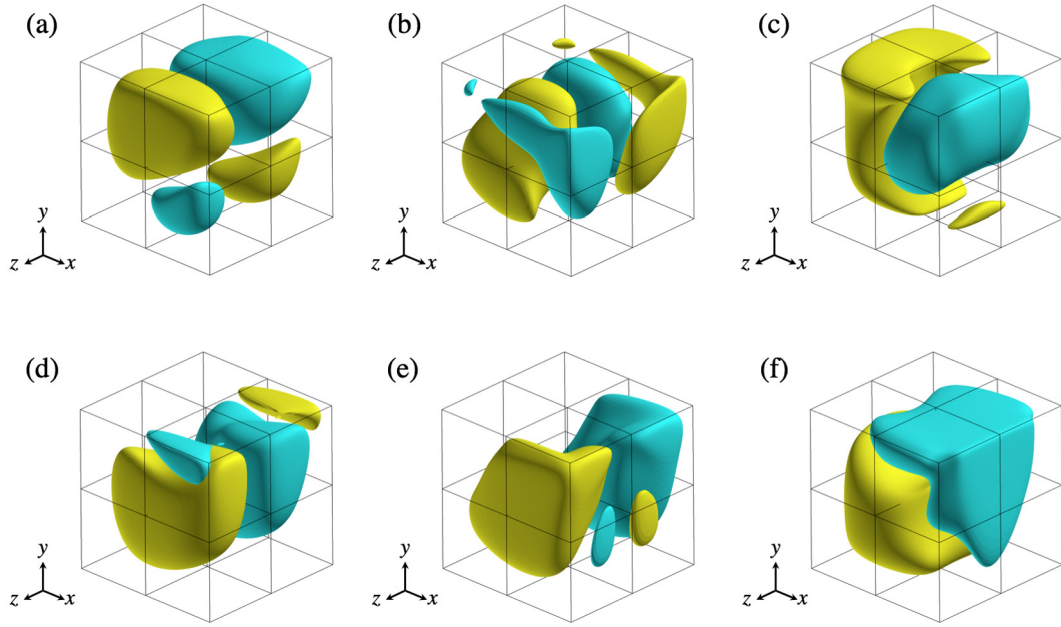
Fig. 5. Direct (a-c) and adjoint (d-f) eigenvectors of the 1st mode of cubic cavity flow analysis. Real parts are shown. Yellow and light blue isosurfaces represent the positive and negative values, respectively. (a, d) Momentum in x direction (b, e) Momentum in y direction. (c, f) Momentum in z direction. (For interpretation of the colors in the figure(s), the reader is referred to the web version of this article.)
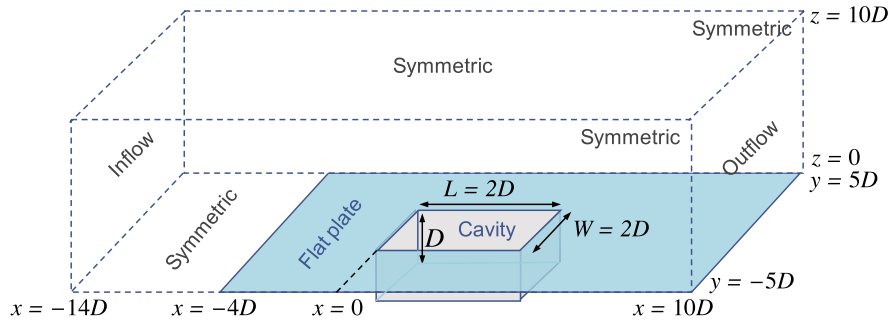

Fig. 6. Computational setup for flow over a finite-width cavity (not to scale).

Table 4
Minimum grid spacing and number of grid points of three computational grids for 3D open cavity flow simulations.

Label	Δ_{min}	Number of grid points ($N_x \times N_y \times N_z$)		Total number of grid points
		Grid inside the cavity	Grid over the plane $z = 0$	
G1	$1.5 \times 10^{-3} D$	$240 \times 160 \times 120$	$720 \times 320 \times 120$	3.22×10^7
G2	$3.0 \times 10^{-3} D$	$210 \times 130 \times 100$	$560 \times 260 \times 100$	1.73×10^7
G3	$5.0 \times 10^{-3} D$	$180 \times 60 \times 70$	$390 \times 120 \times 70$	4.03×10^6

for time integration was chosen so that Courant number, based on the minimum grid spacing and sum of the freestream speed of sound and flow velocity, is equal to 0.9. In this analysis, the selective frequency damping method [39] was used for baseflow calculations to obtain steady flow fields. The computational grid was a nonuniform spaced Cartesian grid. Three computational grids were used to examine the grid dependency. The details are listed in Table 4. The dimension of Krylov subspace m was set to 150 and restart strategy of Krylov-Schur method was utilized in this analysis to obtain converged eigenmodes using small m. For the restart of Krylov-Schur method, 20 least stable modes were used to construct the initial Arnoldi vectors of next iterations. The integration time Δt for time-stepping was set to unity. With this condition, approximately 450 Arnoldi iterations in total were required to obtain sufficient convergence of three least stable eigenmodes.

Table 5

Three least stable eigenvalues ($\sigma \pm St_D i$) obtained with three different computational grids.

	1st mode		2nd mode		3rd mode	
	Direct	Adjoint	Direct	Adjoint	Direct	Adjoint
G1	$0.0384 \pm 0.3563i$	$0.0387 \pm 0.3562i$	$0.0115 \pm 0.2017i$	$0.0113 \pm 0.2013i$	$-0.0108 \pm 0.0165i$	$-0.0108 \pm 0.0165i$
G2	$0.0380 \pm 0.3564i$	$0.0383 \pm 0.3563i$	$0.0118 \pm 0.2017i$	$0.0119 \pm 0.2014i$	$-0.0112 \pm 0.0165i$	$-0.0112 \pm 0.0165i$
G3	$0.0400 \pm 0.3570i$	$0.0402 \pm 0.3569i$	$0.0133 \pm 0.2018i$	$0.0137 \pm 0.2016i$	$-0.0116 \pm 0.0165i$	$-0.0116 \pm 0.0165i$

5.3.2. Results and discussion

Table 5 shows the eigenvalues obtained by the three grids with different resolutions. The direct and adjoint eigenvalues for the three least stable modes are shown. It can be confirmed that the eigenvalues are almost grid independent in the finer grids G1 and G2. The changes in the growth rate and Strouhal number are $\Delta\sigma = O(10^{-4})$ and $\Delta St_L = O(10^{-4})$, respectively, which corresponds to the relative difference of $O(10^{-3})$. The direct and adjoint eigenvalues are in good agreement, and the relative difference between these eigenvalues is $O(10^{-3})$. The CPU time required for the adjoint analysis with the grids G1, G2, and G3 is approximately 40, 11, and 2 hours, respectively, where the hybrid OpenMP and MPI parallelization was implemented and 21 Fujitsu A64FX (2.0 GHz, 48 cores) CPUs were used. The following results were obtained for grid G1, which was the finest grid.

As shown in Table 5, the frequencies of the most unstable mode and the second most unstable mode are $St_D \approx 0.36$ and $St_D \approx 0.20$, respectively. Here, the Strouhal number St_D is a dimensionless frequency based on the freestream velocity and cavity depth D. These frequencies are close to the frequencies of the 2nd Rossiter mode [40,41] $St_D = 0.375$ and the 1st Rossiter mode $St_D = 0.161$. Brès and Colonius [36] and Sun et al. [42] conducted two-dimensional direct numerical simulation (DNS) of open cavity flow with $L/D = 2$ and $M = 0.6$. They obtained the 1st and 2nd Rossiter mode frequencies of $St_D = 0.202$ and 0.349 and $St_D = 0.206$ and 0.358, respectively. This suggests that the 1st and 2nd unstable modes obtained in the present analysis are the modes related to the Rossiter mode, which is the self-sustained oscillation caused by shear layer instability.

Figs. 7 and 8 show the eigenvectors of the 1st direct and adjoint eigenvectors. Figs. 7b and 7e are the distributions of momentum in the x direction and pressure components on $y/D = 0$. It can clearly be seen that this mode represents the instability phenomenon of the shear layer separated from the leading edge of the cavity. This distribution is very similar to that obtained from two-dimensional analysis (BiGlobal stability) by Sun et al. [38]. On the other hand, Figs. 7a, 7d, 7c, and 7f indicate that a three-dimensional distribution appears due to the influence of the sidewalls. The corresponding adjoint mode shows that there is receptivity near the leading edge of the cavity and its upstream region. These findings are expected to become important insights for controlling the cavity oscillation phenomenon.

The 3rd mode is stable and characterized by a low frequency of $St_D = 0.016$. Looking at the x direction momentum component of the eigenvector shown in Fig. 9, it can be seen that there is a longitudinal structure associated with the instability of the main vortex in the cavity. This structure is not completely periodic in the spanwise direction due to the influence of sidewalls, but the wavelength in the spanwise direction is $\lambda_{span} \approx 1D$ (Figs. 9b and 9d). Brès and Colonius [36] reported a mode of $St_D = 0.016$ and $\lambda_{span} = 1D$ from BiGlobal stability analysis, and it is suggested that a similar phenomenon was captured in the present analysis. In addition, they investigated the instability of this flow field at various Mach numbers and Reynolds numbers. According to their study, the flow field is estimated to be unstable in the shear layer (1st and 2nd) modes and stable in the vortex instability (3rd) mode under the flow condition used in the present analysis. This is consistent with the present results.

As demonstrated above, it was confirmed that the developed method can perform large-scale TriGlobal direct and adjoint stability analyses of fully three-dimensional open cavity flow. As a result, it was found that when $L/D = 2$, $W/D = 2$, and $Re_D = 1500$, the similar instability phenomenon found by two-dimensional analysis can occur although there is an influence from the sidewalls. Further investigation is required to elucidate the impact of sidewalls on cavity flow instability. For example, according to the DNS of Sun et al. [42], Rossiter modes are weaker in the presence of sidewalls.

6. Conclusions

In this study, we developed a numerical method for TriGlobal adjoint stability analysis of the compressible Navier–Stokes equations. The developed method is an extension of the global direct stability analysis method by Ohmichi and Suzuki [10] to adjoint stability analysis. That is, the developed method has matrix-free property based on the time-stepping approach, and uses the finite compact difference method for spatial discretization of fluid simulations. Therefore, this method is effective for a large-scale TriGlobal stability analysis because it has a computational memory (RAM) saving property and high-order spatial accuracy. To develop the time-stepping approach for adjoint stability analysis, we performed the cumbersome task of deriving the adjoint equations including the corresponding appropriate boundary conditions for the compressible Navier–Stokes equations. The adjoint equations were derived in this study and it was confirmed that the derived equations are correct and appropriately discretized.

For verification and demonstration, three flow fields were analyzed using the developed method. It was confirmed that the obtained adjoint eigenvalues match their corresponding direct eigenvalues in all test cases. As a first test, the low Mach
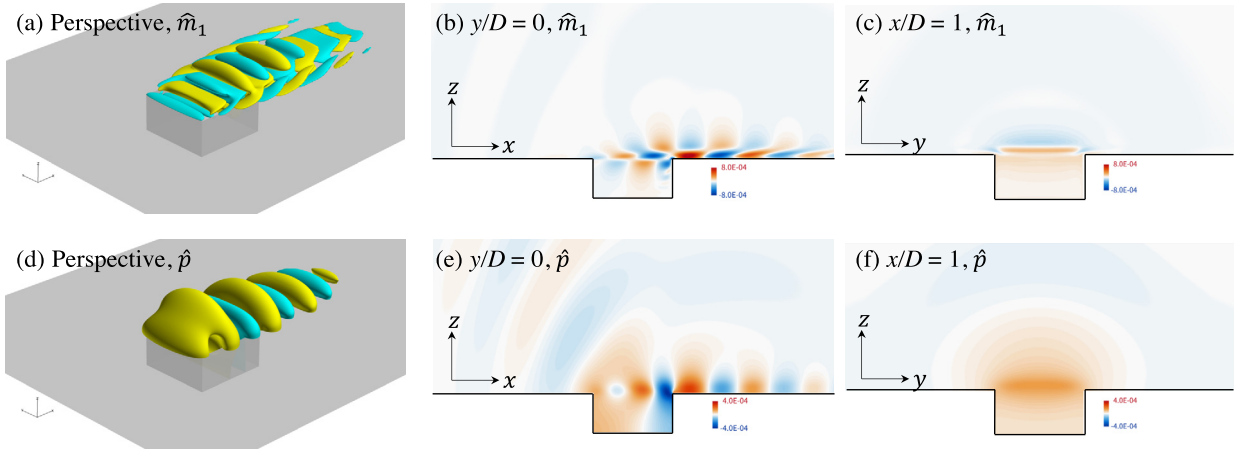
Fig. 7. Eigenvectors of 1st direct mode. Momentum in x direction and pressure components are shown in the top and bottom rows, respectively.
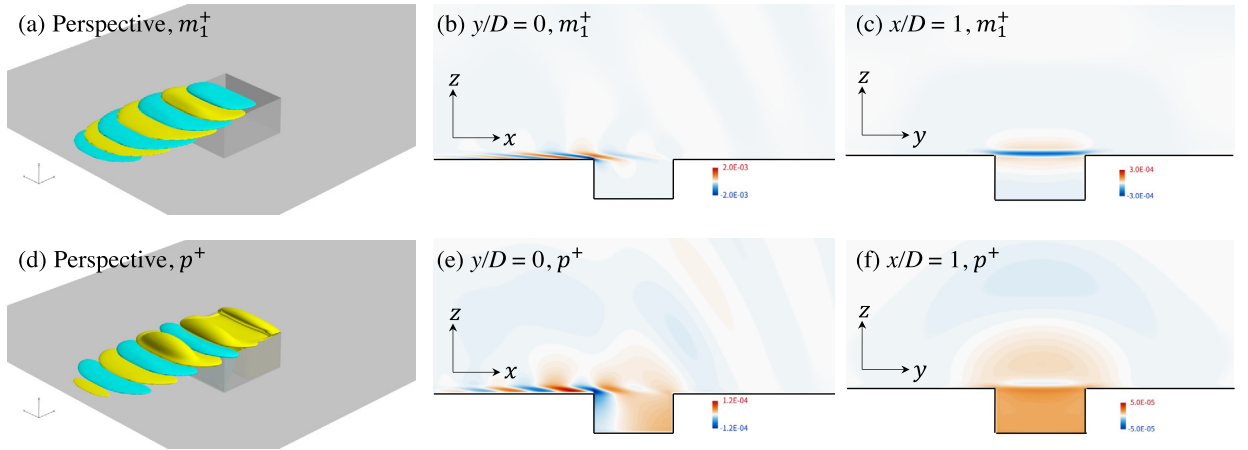

Fig. 8. Eigenvectors of 1st adjoint mode. Momentum in x direction and pressure components are shown in the top and bottom rows, respectively.
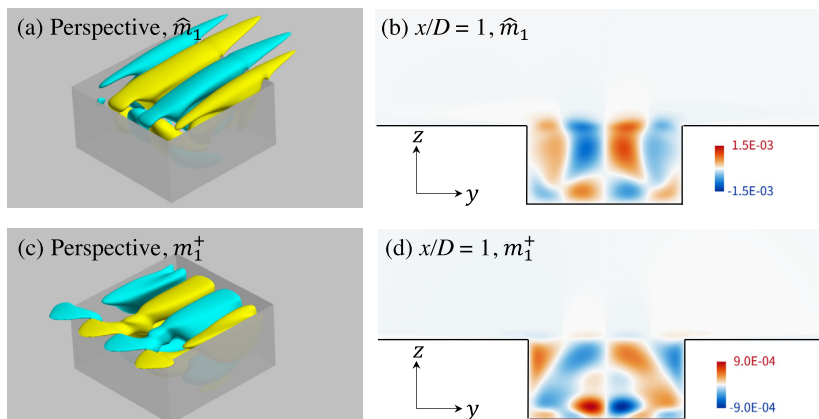

Fig. 9. Eigenvectors of 3rd (a), (b) direct and (c), (d) adjoint modes. The component of the momentum in the x direction is shown.

number two-dimensional flow past a square cylinder was analyzed. It was confirmed that the obtained adjoint mode was in agreement with the results of previous studies obtained by incompressible fluid analysis. Furthermore, the receptivity and sensitivity regions of the SW mode (namely the far wake mode) were clarified. Secondly, a cubic lid-driven cavity flow analysis was conducted as a test case for the simple fully three-dimensional flow field, and it was confirmed that the eigenvalues of the direct and adjoint modes obtained with the developed method agree well with the direct mode found in previous research [35]. Finally, three-dimensional open cavity flow was analyzed, and we showed that large-scale TriGlobal analysis with order of 10^7 grid points is possible. This is the first time that TriGlobal direct and adjoint stability analyses for compressible open cavity flow have been conducted. The results show that in the case of $L/D = 2$, $W/D = 2$, and $Re_D = 1500$, the similar instability phenomenon as in the case of the two-dimensional analysis can appear, although sidewall effects exist. The sidewall effects will be investigated in more detail in future work.

CRediT authorship contribution statement

Yuya Ohmichi: Conceptualization, Data curation, Funding acquisition, Investigation, Methodology, Software, Validation, Visualization, Writing – original draft, Writing – review & editing. **Kento Yamada:** Investigation, Methodology, Software, Validation, Writing – original draft, Writing – review & editing.

Declaration of competing interest

The authors declare that they have no known competing financial interests or personal relationships that could have appeared to influence the work reported in this paper.

Acknowledgements

Appendix A. Derivation of LODI relations for adjoint variables

We derive the LODI relations (61) for the adjoint variables in this section. If we ignore the viscous terms and multi-dimensional effect other than in the x direction, the adjoint compressible Navier–Stokes equations can be simplified as follows:

$$\frac{\partial \boldsymbol{q}^*}{\partial t} + \boldsymbol{A}\frac{\partial \boldsymbol{q}^*}{\partial x} = \boldsymbol{0} \tag{67}$$

where

$$\boldsymbol{A} = \begin{pmatrix} 0 & \bar{u}^2 & 0 & 0 & \bar{c}^2\bar{u} \\ -1 & -2\bar{u} & 0 & 0 & -\bar{c}^2 \\ 0 & 0 & -\bar{u} & 0 & 0 \\ 0 & 0 & 0 & -\bar{u} & 0 \\ 0 & -1 & 0 & 0 & -\bar{u} \end{pmatrix}. \tag{68}$$

Using the matrix $\boldsymbol{S}$ whose columns are the right eigenvectors of $\boldsymbol{A}$ and its inverse $\boldsymbol{S}^{-1}$ whose rows are the left eigenvectors of $\boldsymbol{A}$, $\boldsymbol{A}$ can be diagonalized as $\boldsymbol{S}^{-1}\boldsymbol{A}\boldsymbol{S} = \boldsymbol{\Lambda}^*$, where $\boldsymbol{\Lambda}^*$ is the diagonal matrix whose components are shown in (64). With this matrix relation, Equation (67) can be rewritten as

$$\frac{\partial \boldsymbol{q}^*}{\partial t} + \boldsymbol{S}\boldsymbol{L}^* = \boldsymbol{0} \tag{69}$$

The $\boldsymbol{L}^*$ in the second term on the left side of the equation represents the characteristic wave amplitude defined as

$$\boldsymbol{L}^* = \boldsymbol{\Lambda}^*\boldsymbol{S}^{-1}\frac{\partial \boldsymbol{q}^*}{\partial x}. \tag{70}$$

The components of $\boldsymbol{L}^*$ are shown in (63), and $\boldsymbol{S}$ and $\boldsymbol{S}^{-1}$ are

$$\boldsymbol{S} = \begin{pmatrix} \bar{c}\bar{u} & -\bar{c}^2 & 0 & 0 & -\bar{c}\bar{u} \\ -\bar{c} & 0 & 0 & 0 & \bar{c} \\ 0 & 0 & 1 & 0 & 0 \\ 0 & 0 & 0 & 1 & 0 \\ 1 & 1 & 0 & 0 & 1 \end{pmatrix} \tag{71}$$

and

$$\boldsymbol{S}^{-1} = \frac{1}{2\bar{c}^2} \begin{pmatrix} 1 & \bar{u} - \bar{c} & 0 & 0 & \bar{c}^2 \\ -2 & -2\bar{u} & 0 & 0 & 0 \\ 0 & 0 & 2\bar{c}^2 & 0 & 0 \\ 0 & 0 & 0 & 2\bar{c}^2 & 0 \\ 1 & \bar{u} + \bar{c} & 0 & 0 & \bar{c}^2 \end{pmatrix}. \tag{72}$$

The derived Equation (69) is identical to (61) from (70)–(72).

References

[1] V. Theofilis, Global linear instability, Annu. Rev. Fluid Mech. 43 (2011) 319–352, https://doi.org/10.1146/annurev-fluid-122109-160705.

[2] F. Gómez, S.L. Clainche, P. Paredes, M. Hermanns, V. Theofilis, Four decades of studying global linear instability: progress and challenges, AIAA J. 50 (12) (2012) 2731–2743, https://doi.org/10.2514/1.J051527.

[3] D.C. Hill, A theoretical approach for analyzing the restabilization of wakes, in: 30th Aerospace Sciences Meeting and Exhibit, Reno, NV, U.S.A, 1992.

[4] F. Giannetti, P. Luchini, Structural sensitivity of the first instability of the cylinder wake, J. Fluid Mech. 581 (2007) 167–197, https://doi.org/10.1017/S0022112007005654.

[5] O. Marquet, D. Sipp, L. Jaquin, Sensitivity analysis and passive control of cylinder flow, J. Fluid Mech. 615 (2008) 221–252, https://doi.org/10.1017/S0022112008003662.

[6] P. Meliga, D. Sipp, J.M. Chomaz, Effect of compressibility on the global stability of axisymmetric wake flows, J. Fluid Mech. 660 (2010) 499–526, https://doi.org/10.1017/S002211201000279X.

[7] J.W. Nichols, S.K. Lele, Global modes and transient response of a cold supersonic jet, J. Fluid Mech. 669 (2011) 225–241, https://doi.org/10.1017/S0022112010005380.

[8] S. Chiba, Global stability analysis of incompressible viscous flow, J. Jpn. Soc. Comput. Fluid Dyn. 7 (1) (1998) 20–48.

[9] C.J. Mack, P.J. Schmid, A preconditioned Krylov technique for global hydrodynamic stability analysis of large-scale compressible flows, J. Comput. Phys. 229 (3) (2010) 541–560, https://doi.org/10.1016/j.jcp.2009.09.019.

[10] Y. Ohmichi, K. Suzuki, Assessment of global linear stability analysis using a time-stepping approach for compressible flows, Int. J. Numer. Methods Fluids 80 (10) (2016) 614–627, https://doi.org/10.1002/fld.4166.

[11] Y. Ohmichi, K. Suzuki, Compressibility effects on the first global instability mode of the vortex formed in a regularized lid-driven cavity flow, Comput. Fluids 145 (2017) 1–7, https://doi.org/10.1016/j.compfluid.2016.12.008.

[12] A. Sansica, J.-C. Robinet, F. Alizard, E. Goncalves, Three-dimensional instability of a flow past a sphere: Mach evolution of the regular and Hopf bifurcations, J. Fluid Mech. 855 (2018) 1088–1115, https://doi.org/10.1017/jfm.2018.664.

[13] B. Bugeat, J.-C. Chassaing, J.-C. Robinet, P. Sagaut, 3D global optimal forcing and response of the supersonic boundary layer, J. Comput. Phys. 398 (2019) 108888, https://doi.org/10.1016/j.jcp.2019.108888.

[14] R. Ranjan, S. Unnikrishnan, D. Gaitonde, A robust approach for stability analysis of complex flows using high-order Navier-Stokes solvers, J. Comput. Phys. 403 (2020) 109076, https://doi.org/10.1016/j.jcp.2019.109076.

[15] M.F. de Pando, D. Sipp, P.J. Schmid, Efficient evaluation of the direct and adjoint linearized dynamics from compressible flow solvers, J. Comput. Phys. 231 (23) (2012) 7739–7755, https://doi.org/10.1016/j.jcp.2012.06.038.

[16] J. Crouch, A. Garbaruk, D. Magidov, Predicting the onset of flow unsteadiness based on global instability, J. Comput. Phys. 224 (2) (2007) 924–940, https://doi.org/10.1016/j.jcp.2006.10.035.

[17] J.D. Crouch, A. Garbaruk, M. Strelets, Global instability in the onset of transonic-wing buffet, J. Fluid Mech. 881 (2019) 3–22, https://doi.org/10.1017/jfm.2019.748.

[18] L.E. Eriksson, A. Rizzi, Computer-aided analysis of the convergence to steady state of discrete approximation to Euler equations, J. Comput. Phys. 57 (1) (1985) 90–128, https://doi.org/10.1016/0021-9991(85)90054-3.

[19] S.K. Lele, Compact finite difference schemes with spectral-like resolution, J. Comput. Phys. 103 (1) (1992) 16–42, https://doi.org/10.1016/0021-9991(92)90324-R.

[20] J.D. Müller, P. Cusdin, On the performance of discrete adjoint CFD codes using automatic differentiation, Int. J. Numer. Methods Fluids 47 (2005) 939–945, https://doi.org/10.1002/fld.885.

[21] W.E. Arnoldi, The principle of minimized iterations in the solution of the matrix eigenvalue problem, Q. Appl. Math. 9 (17) (1951) 17–29.

[22] Y. Saad, Variations on Arnoldi's method for computing eigenelements of large unsymmetric matrices, Linear Algebra Appl. 34 (1980) 269–295, https://doi.org/10.1016/0024-3795(80)90169-X.

[23] G.W. Stewart, A Krylov–Schur algorithm for large eigenproblems, SIAM J. Matrix Anal. Appl. 23 (2001) 601–614, https://doi.org/10.1137/S0895479800371529.

[24] R. Lehoucq, D.C. Sorensen, Y. Chao, ARPACK User's Guide: Solution of Large-Scale Eigenvalue Problems with Implicitly Restarted Arnoldi Methods, SIAM, 1997.

[25] J.J. Otero, A.S. sharma, R.D. Sandberg, Direct numerical simulations for adjoint-based optimal flow and noise control of a backward-facing step, in: 22nd AIAA/CEAS Aeroacoustics Conference, Lyon, France, 2016, AIAA 2016–2889, https://doi.org/10.2514/6.2016-2889.

[26] M.R. Visbal, D.V. Gaitonde, On the use of higher-order finite-difference schemes on curvilinear and deforming meshes, J. Comput. Phys. 181 (1) (2002) 155–185, https://doi.org/10.1006/jcph.2002.7117.

[27] D.V. Gaitonde, M.R. Visbal, Padé-type high-order boundary filters for the Navier–Stokes equations, AIAA J. 38 (11) (2000) 2103–2112, https://doi.org/10.2514/2.872.

[28] C.-W. Shu, S. Osher, Efficient implementation of essentially non-oscillatory shock-capturing schemes, J. Comput. Phys. 77 (2) (1988) 439–471, https://doi.org/10.1016/0021-9991(88)90177-5.

[29] K.W. Thompson, Time dependent boundary conditions for hyperbolic systems, J. Comput. Phys. 68 (1) (1987) 1–24, https://doi.org/10.1016/0021-9991(87)90041-6.

[30] T. Poinsot, S. Lele, Boundary conditions for direct simulations of compressible viscous flows, J. Comput. Phys. 101 (1) (1992) 104–129, https://doi.org/10.1016/0021-9991(92)90046-2.

[31] A. Verma, S. Mittal, A new unstable mode in the wake of a circular cylinder, Phys. Fluids 23 (2011) 121701, https://doi.org/10.1063/1.3664869.

[32] G. Tu, Q. Yang, J. Chen, X. Yuan, Preliminary conception and test of global stability decomposition for flow stability analysis, in: Tenth International Conference on Computational Fluid Dynamics (ICCFD10), ACM Press, Barcelona, Spain, 2018, ICCFD10–107.

[33] W. Zhang, R. Samtaney, BiGlobal linear stability analysis on low-Re flow past an airfoil at high angle of attack, Phys. Fluids 28 (4) (2016) 044105, https://doi.org/10.1063/1.4945005.

[34] P.J. Strykowski, K.R. Sreenivasan, On the formation and suppression of vortex 'shedding' at low Reynolds numbers, J. Fluid Mech. 218 (1990) 71–107, https://doi.org/10.1017/S0022112090000933.

[35] V. Theofilis, The linearized pressure Poisson equation for global instability analysis of incompressible flows, Theor. Comput. Fluid Dyn. 31 (5) (2017) 623–642, https://doi.org/10.1007/s00162-017-0435-z.

[36] G.A. Brès, T. Colonius, Three-dimensional instabilities in compressible flow over open cavities, J. Fluid Mech. 599 (2008) 309–339, https://doi.org/10.1017/S0022112007009925.

[37] Y. Sun, K. Taira, L.N. Cattafesta, L.S. Ukeiley, Spanwise effects on instabilities of compressible flow over a long rectangular cavity, Theor. Comput. Fluid Dyn. 31 (5) (2017) 555–565, https://doi.org/10.1007/s00162-016-0412-y.

[38] Y. Sun, K. Taira, L.N. Cattafesta, L.S. Ukeiley, Biglobal instabilities of compressible open-cavity flows, J. Fluid Mech. 826 (2017) 270–301, https://doi.org/10.1017/jfm.2017.416.

[39] E. Åkervik, L. Brandt, D.S. Henningson, J. Hœpffner, O. Marxen, P. Schlatter, Steady solutions of the Navier-Stokes equations by selective frequency damping, Phys. Fluids 18 (6) (2006) 068102, https://doi.org/10.1063/1.2211705.

[40] J.E. Rossiter, Wind tunnel experiments of the flow over rectangular cavities at subsonic and transonic speeds, ARCR & M (1968) 3458.

[41] H. Heller, D. Holmes, E. Covert, Flow-induced pressure oscillations in shallow cavities, J. Sound Vib. 18 (4) (1971) 545–553, https://doi.org/10.1016/0022-460X(71)90105-2.

[42] Y. Sun, Q. Liu, L.N. Cattafesta, L.S. Ukeiley, K. Taira, Effects of sidewalls and leading-edge blowing on flows over long rectangular cavities, AIAA J. 57 (1) (2019) 106–119, https://doi.org/10.2514/1.J057413.